Nonlinear dynamics of semiconductor lasers with active optical feedback

S. Bauer,* O. Brox, J. Kreissl, and B. Sartorius
Fraunhofer-Institut for Telecommunications, Heinrich-Hertz-Institut, Einsteinufer 37, 10587 Berlin, Germany

M. Radziunas
Weierstraß-Institut für Angewandte Analysis und Stochastik, Mohrenstrasse 39, 10117 Berlin, Germany

J. Sieber
Department of Engineering Mathematics, University of Bristol, University Walk, Bristol BS8 1TR, United Kingdom

H.-J. Wünsche and F. Henneberger
Mathematisch-Naturwissenschaftliche Fakultät 1, Institut für Physik, Humboldt-Universität zu Berlin, Newtonstrasse 15, 12489 Berlin, Germany

(Received 31 July 2003; published 27 January 2004)

An in-depth theoretical as well as experimental analysis of the nonlinear dynamics in semiconductor lasers with active optical feedback is presented. Use of a monolithically integrated multisection device of submillimeter total length provides access to the short-cavity regime. By introducing an amplifier section as a special feature, phase and strength of the feedback can be separately tuned. In this way, the number of modes involved in the laser action can be adjusted. We predict and observe specific dynamical scenarios. Bifurcations mediate various transitions in the device output, from single-mode steadystate to self-pulsation and between different kinds of self-pulsations, reaching eventually chaotic behavior in the multimode limit.

DOI: 10.1103/PhysRevE.69.016206 PACS number(s): 05.45.−a, 42.55.Px

I. INTRODUCTION

Semiconductor lasers with optical feedback are both of fundamental and practical importance. In a general sense, these lasers belong to the class of delay systems, extensively studied in many different areas. The nonlocal time evolution caused by the feedback creates—in combination with the nonlinearity of the laser—new dynamical regimes. Phenomena such as low- and high-frequency oscillations, coherence collapse [1], excitability [2–4], and other effects have recently been predicted and experimentally observed. Potential applications are high-speed data transmission [5], cryptography [6], etc. However, practical devices require proper control of the complexity and, associated with this, a systematic understanding of the various nonlinear dynamical scenarios. The subject of this paper is a special laser structure, where the feedback is amplified by using an active medium in the external cavity. We will demonstrate that this active feedback laser (AFL) exhibits various advantages as it allows one to tune the feedback level and, in this way, to adjust the system close to a desired bifurcation point.

Optical feedback is usually achieved by combining the laser with an external mirror. The characteristic parameters are (i) the delay time τ through the round trip in the external cavity, (ii) the intensity fraction K^2 that reenters the laser, and (iii) the phase ϕ of the feedback field. The solitary laser is supposed to run in a single-mode continuous-wave (cw) regime. The behavior in the presence of feedback crucially depends on the number of modes that are of relevance in the compound device. This number grows when the feedback strength K increases. A second factor arises through the time scales involved. Photon lifetimes in typical semiconductor lasers are $\tau_p \approx 1-10$ ps, while the period of the relaxation oscillations τ_R ranges between 0.1 and 1 ns at reasonable injection levels. In the long-cavity limit, addressed in most previous studies, τ is much longer than τ_R. The solitary mode is hence transformed in a quasicontinuous spectrum of external cavity modes, even for modest K. The consequence is an irregular dynamical response with stochastic power dropouts. A recent study on shorter cavities ($\tau/\tau_R \approx 1$) has yielded qualitatively different behavior [7,8]. Here, the feedback phase begins to influence the field-inversion dynamics in the laser. Regular pulse packages have been observed which originate from a global trajectory along a limited number of modes in the phase-inversion space.

Distributed feedback (DFB) structures, where laser and external cavity are monolithically integrated in a single device, enable one to access the limit of very short cavities. Here, the length of both laser and feedback section is in the 100 μm range resulting in $\tau/\tau_R \approx 0.01$. In this situation, distinct beating phenomena, associated with mode-antimode pairs, are expected [9]. However, their occurrence requires sufficiently strong feedback. In external-mirror arrangements K is restricted to levels of about 0.1. In order to overcome this limitation, we have developed a device [10] schematically depicted in Fig. 1. It combines a DFB laser with an active feedback cavity (AFC). For separate control of feedback phase and amplitude, the AFC comprises a phase tuning as well as an amplifier section, both independently biased. Current injection in the phase tuning section with larger band gap modifies the refractive index by free-carrier transitions. The amplifier section is similarly designed as the laser, omitting however the DFB grating and leaving the end facet un-

*Electronic address: bauer@hhi.fraunhofer.de

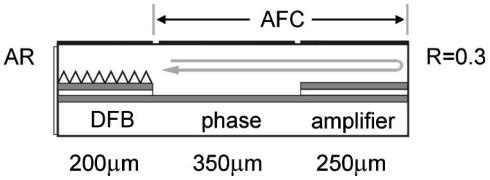

FIG. 1. Schematics of the AFL used in this study. The combination of separate phase and amplifier sections allows for an independent phase and amplitude control of the feedback. AR, antireflection coated; *R*, facet power reflectivity.

coated for mirror action. With the AFC, the feedback strength K can be tuned in a range between 10^{-2} and nearly 1.

The paper is organized as follows. In the first part, we present a theoretical analysis of the AFL. After introduction of the traveling wave equations and the relevant device parameters, the optical mode spectrum at different feedback levels is investigated. A subsequent full numerical solution reveals the characteristic dynamical regimes of the AFL. Based on the fact that only one or two modes contribute essentially to the dynamics, a systematic bifurcation analysis is finally performed. In the second, experimental part, we focus mainly on the regions of nonstationary device output. Our findings are in very good qualitative and quantitative agreement with the theoretical predictions. We observe single-mode pulsations at low feedback as well as mode-beating (MB) pulsations in the high-feedback range. The highly nonlinear behavior of the AFL is demonstrated by the occurrence of torus-type oscillations and hysteresis for proper choice of the feedback parameters.

II. THEORETICAL ANALYSIS

For a number of reasons, the standard Lang-Kobayashi mean-field equations [11] do not provide an appropriate description of the AFL. First, feedback cavity and laser section have comparable length extensions. Second, representing the focus of our study, the feedback is not weak and, hence, cannot be considered as a small perturbation. Third, not only the carriers in the laser but also those in the amplifier interact with the optical field. This produces nonlinearities and memory effects in the feedback so that the delay cannot be characterized by a single time constant. All these factors give rise to a complex spatio-temporal structure across the compound device which have to be properly addressed. This is achieved by using traveling wave equations, which have been developed for studying multisection DFB lasers (see, e.g., Refs. [5,12,13]). Though their degree of complexity is high, systematic investigations for a variety of different devices over the last years enable today a reliable handling, both regarding the relevant physical processes as well as the relatively large parameter set.

A. Traveling wave equations

The slowly varying envelopes $E_{\pm}(t,z)$ of the forward and backward traveling waves obey the equations

$$\left(-\frac{i}{v_g}\frac{\partial}{\partial t}\mp i\frac{\partial}{\partial z}+\beta-i\frac{\alpha}{2}\right)E_{\pm}+\kappa E_{\mp}=0, \tag{1}$$

where v_g is the group velocity, α the absorption coefficient for parasitic losses, and κ the coupling coefficient of the DFB gratings. Boundary conditions are $E_{+}(t,0)=0$ at the antireflection coated DFB facet and $E_{-}(t,L)=\sqrt{R}E_{+}(t,L)$ at the cleaved facet of the feedback cavity. The waveguide propagation parameter β is a constant in the passive phase tuning section. For a length l_P, it is given by

$$\beta=-\frac{\phi_P}{2l_P}, \tag{2}$$

where the phase shift ϕ_P represents one of the externally controllable bifurcation parameters of the AFL dynamics.

In the active sections, β is a function of t and z and contains the following contributions:

$$\beta=\delta+(i+\alpha_H)\frac{g}{2}-i\mathcal{D}. \tag{3}$$

Here, δ is the background wave number measured relative to the Bragg resonance and α_H denotes the linewidth enhancement factor. The peak gain g is a function of the carrier density N,

$$g=\frac{g'(N-N_{\mathrm{tr}})}{1+\varepsilon S}, \quad S=|E_{+}|^2+|E_{-}|^2, \tag{4}$$

with g' as differential gain, including the transverse confinement factor, N_{tr} as transparency concentration, and ε accounting for nonlinear gain saturation. The optical field is normalized so that S represents the local photon density. Dispersive contributions are taken into consideration by the operator $\mathcal{D}$ reading as

$$\mathcal{D}E_{\pm}=\frac{\overline{g}}{2}(E_{\pm}-p_{\pm}). \tag{5}$$

For the polarization $p_{\pm}$, a single-oscillator model is used:

$$-i\frac{\partial}{\partial t}p_{\pm}=-i\overline{\gamma}(E_{\pm}-p_{\pm})+\overline{\omega}p_{\pm}, \tag{6}$$

where $\overline{\omega}$ is the resonance frequency taken relative to the central frequency $2\pi c/\lambda_0$, $g-\overline{g}$ the off-resonance gain, and $\overline{\gamma}$ measures the gain bandwidth [13].

The carrier densities $N(t,z)$ in the DFB and amplifier section are solutions of the rate equation

$$\frac{\partial}{\partial t}N=J-r(N)-v_g\sum_{\nu=\pm}\mathrm{Im}[E_{\nu}\beta E_{\nu}]. \tag{7}$$

The terms on the right-hand side are the injection rate J, the spontaneous recombination $r(N)=AN+BN^2+CN^3$, as well as the stimulated emission. Note that neither carrier diffusion nor forward-backward wave interferences (e.g., $\sim E_{+}\beta E_{-}$) appear. The spatial period of the latter is shorter by more

TABLE I. Parameter values used for the DFB, phase tuning (P), and amplifier (A) sections.

	Explanation	Values			Unit
		DFB	P	A	
κ	Index coupling coefficient	130	0	0	cm^{-1}
l	Section length	200	350	250	μm
σ	Cross section of AZ	0.45		0.45	$\mu\mathrm{m}^2$
g'	Effective differential gain	9		9	$10^{-17}\ \mathrm{cm}^2$
α_H	Henry factor	-5		-5	
α	Internal absorption	25	[20,40]	25	cm^{-1}
δ	Static detuning	402.7		[0,160]	cm^{-1}
I	Current injection	70		[0,100]	mA
N_{tr}	Transparency carrier density	1		1	$10^{18}\ \mathrm{cm}^{-3}$
A	Recombination coefficient	0.3		0.3	$10^{9}\ \mathrm{s}^{-1}$
B	Recombination coefficient	1		1	$10^{-10}\ \mathrm{cm}^3\,\mathrm{s}^{-1}$
C	Recombination coefficient	1		1	$10^{-28}\ \mathrm{cm}^6\,\mathrm{s}^{-1}$
ε	Nonlinear gain component	3		3	$10^{-18}\ \mathrm{cm}^3$
U_F'	Differential Fermi level separation	1		1	$10^{-19}\ \mathrm{V/cm}^3$
R_s	Series resistivity	5		5	Ω
$\overline{g}$	Lorentzian weight	200	0	200	cm^{-1}
$\overline{\gamma}$	Lorentzian half-width	23.84		23.84	rad/ps
$\overline{\omega}$	Lorentzian central frequency	2.384		2.384	rad/ps
λ_0	Central wavelength	1540			nm
R	Power reflectivity			0.3	
v_g	Group velocity		$c/3.8$		

than an order of magnitude compared to the diffusion length and thus not transferred to the carrier density. On the other hand, after having dropped these mixed terms, the stimulated recombination varies on a scale much longer than the diffusion length, with the consequence that diffusion can be dropped, too. Longitudinal spatial hole burning (LSHB) associated with long-scale modulations of the stimulated emission rate is essential for DFB lasers. However, LSHB is counteracted by current redistribution [14], which we describe by an inhomogeneous injection rate

$$J(t,z)=\frac{I}{e\sigma l}-\frac{U_F'}{e\sigma l R_s}(N-\langle N\rangle) \quad (z\in \text{ active section}), \tag{8}$$

where all quantities (I, injection current; l, section length; σ, cross section of active zone (AZ); U_F', differential Fermi level separation; R_s, series resistivity, and $\langle N\rangle$, average carrier density over one section) have to be specified for laser and amplifier section.

Apart from resonant contributions, current injection modifies also the background parameters α and δ. In this work, we restrict ourselves to a fixed bias in the laser section so that these parameters are not subject to change. Previous investigations [15] have shown that the loss in the phase section (α_P) is in good approximation a linear function of the phase shift ϕ_P. For the present AFL device, a proper choice is $\alpha_P=20\ \mathrm{cm}^{-1}+5\ \mathrm{cm}^{-1}(\phi_P/2\pi)$. In the amplifier section, the direct carrier-induced change of the gain coefficient is by far dominant so that we can ignore a modification of the background losses. However, current heating alters significantly the background detuning. Following Ref. [15], we take this into account by assuming $\delta_A=\beta_{th}I_A/l_A$ with the thermal detuning coefficient $\beta_{th}=40\ \mathrm{A}^{-1}$. Table I collects the values of device parameters used throughout this paper. The use of different values will be noted in the text.

A reasonable definition of the feedback strength in the AFL is

$$K=\sqrt{R}\,\exp[-\alpha_P L_P+(g_A-\alpha_A)L_A], \tag{9}$$

where g_A is taken at the average density $\langle N_A\rangle$. The upper limit for K is set by the onset of gain saturation.

B. Optical modes

Mode analysis is a key to understanding the effects of feedback on the dynamics of a laser. The optical modes of the hot compound cavity are defined as the set of solutions of an eigenvalue equation following from Eqs. (1) and (6) when substituting the time derivatives $-i\partial/\partial t$ by the complex algebraic factor Ω. For comparing different feedback levels, we tune $\langle N_A\rangle$ and by this the gain in the amplifier section like an external parameter, while the density in the DFB section is kept fixed at the solitary laser level. Real and imaginary parts of the eigenvalues Ω define wavelength and damping of the modes, respectively. Full solution of the steady-state carrier density equation is possible but less instructive.

Figure 2(a) illustrates the change of the mode spectrum under feedback and the role of amplification. Most dramatic in comparison with the solitary DFB laser is the appearance

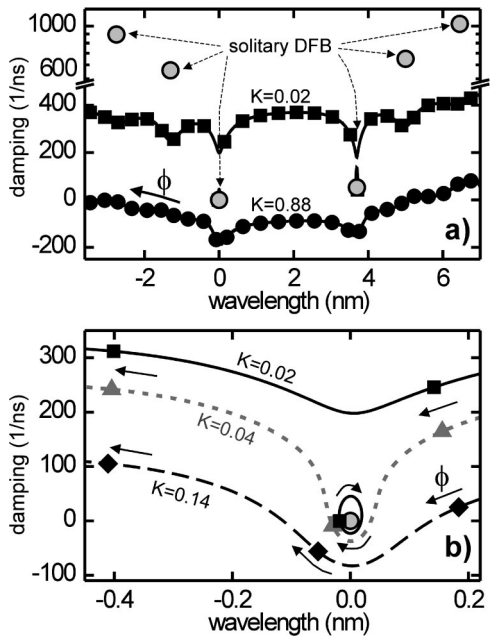

FIG. 2. Spectrum of optical modes of an AFL. (a) Overview; (b) environment of the lasing mode. Bullets: solitary laser ($K=0$). Full symbols: $K=0.02, 0.04, 0.14$, and 0.88, calculated under the following $\varepsilon=0$, no LSHB, feedback phase fixed. Lines: locations of modes for all possible feedback phases ϕ. Arrows: direction of increasing ϕ. After one phase period, each mode replaces its formerly next neighbor on the same line.

of a comb of nearly equidistant compound cavity modes. The 0.4 nm average spacing of these new modes is consistent with the 800 μm total cavity length and almost independent of the amplifier gain. Apparently, a Fabry-Perot(FP)-like cavity is formed by the reflecting amplifier facet on one side and the DFB grating on the other side. In contrast to their spacing, the damping of the FP-type modes depends strongly on the feedback strength. For $K=0.02$, corresponding to $I_A \approx 0$ mA, the decay times are shorter than 5 ps and, therefore, these modes are not essential for the device dynamics. However, the mode damping is strongly reduced with increasing amplification. Negative values, as occurring for the largest feedback in Fig. 2(a), are an artifact caused by the constraint of fixed N in the DFB section. If this constraint is relaxed, N will adjust until the damping of the mode with the lowest loss reaches the minimum value of zero.

Besides creating additional FP-like modes, the feedback also influences the lasing mode as shown in Fig. 2(b). For low feedback, this influence is weak. When tuning the feedback phase by one period, the lasing mode moves around an ellipse in the damping—wavelength plane. In parallel, the FP-type modes of much higher damping move along a separate nonclosed line, replacing the formerly next neighbor after one period. Single-mode dynamics is expected in this regime. With increasing feedback, the ellipse blows up until it touches the FP-like branch and merges with it in a similar way as already described for a double-cavity laser [16]. Beyond this amplification, all modes are located on a single open line, exhibiting a deep valley close to the wavelength of the solitary laser. When increasing the feedback phase, the

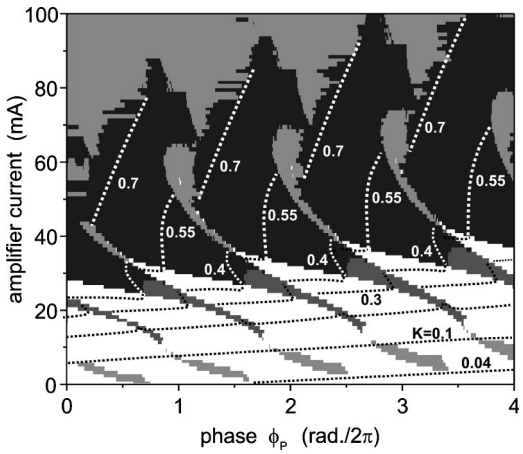

FIG. 3. Calculated areas of self-pulsations in the plane spanned by the two parameters ϕ_P and I_A. The DFB injection level was fixed to $I_{\mathrm{DFB}}=70$ mA, the damping in the phase section is increased by 5/cm per 2π. White areas correspond to cw output. Different levels of gray indicate nonstationary output with frequencies f (main peak of power spectrum) in the following ranges: $f<15$ GHz (light), 15 GHz$<f<$30 GHz (dark), and $f>30$ GHz (black). Dotted lines represent curves of constant K (averaged over one pulsation period in the self-pulsation areas).

modes move from right to left through this valley and take over lasing as long as they are the one of lowest damping. This repeats with a period of 2π, always with a new mode. As the new mode moves down, its predecessor climbs up on the opposite side of the valley. In a certain phase range, both modes have comparable damping and contribute to the laser dynamics. Stronger amplification makes the valley less distinct so that even more than two modes come into play. An important feature of active feedback is therefore the ability to adjust the number of modes involved in the laser dynamics.

C. Full numerical solution

After having gained qualitative insight in the mode spectrum, a full numerical solution of the traveling wave equations is performed for the AFL device experimentally studied below. External bifurcation parameters are the amplifier current I_A and the phase shift ϕ_P [Eq. (2)] adjusted via the current I_P on the passive section. When changing these parameters, the laser output undergoes various transitions, from steady state to self-pulsations, or between self-pulsations of different frequencies. The numerical results are summarized in Fig. 3 by a contour plot in the (ϕ_P, I_A) plane, where the gray scale represents the frequency of the self-pulsations. All calculations were performed for increasing phase direction, i.e., only bifurcations occurring in this direction are accounted for. The behavior is not fully periodic when tuning ϕ_P over several 2π cycles. Islands of given pulsation frequency f shift slightly upwards, as the losses in the phase section linearly increase with ϕ_P (cf. Sec. II A). The tilt of the islands manifests the amplifier contribution to the feedback phase. It is negative for low I_A, because the growing inversion reduces the refractive index. At about 50 mA, the inversion saturates and the remaining thermal effects cause a small opposite tilt.

At least four different dynamical regimes can be recognized. At low currents (I_A up to $\approx$10 mA), small islands of low-frequency self-pulsations appear (regime I). Above a small gap, regime II starts, characterized by narrow stripes of self-pulsations with distinctly higher frequencies. For even larger I_A, the frequencies increase and the stripes widen. In regime III, established between about 30 and 80 mA, self-pulsations with frequencies above 30 GHz fill nearly the whole phase period. The different periods are separated by narrow stripes with lower frequencies. At highest amplification levels (regime IV), low-frequency pulsations dominate again.

The four regimes are closely related to the evolution of the optical mode spectrum sketched in Fig. 2. We have analyzed this correlation by decomposing the numerically calculated fields $E_{\pm}(z,t)$ into instantaneous modes of the hot compound cavity. In regime I, only one mode essentially contributes to the pulsating states. A jump to the next FP-type mode appears in every period at the right-hand edge of the pulsation islands. The old mode and the new mode coexist in the beating-type pulsations of regime II and in the high-frequency pulsations of regime III. Each island belongs to a definite pair of such master modes. Different islands correspond to different pairs. More than two modes participate in the irregular low-frequency pulsations of regime IV as well as in the narrow stripes of regime III. Accordingly, the pulsations here are irregular in most points of operation.

The regimes also differ with respect to the feedback strength. K is mainly determined by the amplifier current only in the single-mode regions of cw states or type-I pulsations, where the lines of constant K in Fig. 3 are nearly horizontal. The lower and upper boundaries of the single-mode pulsations are roughly given by $K=0.04$ and $K=0.1$, respectively. In contrast, the lines of constant K are almost vertical in the MB pulsation regimes II and III, i.e., K is determined by ϕ_P and no longer controlled by the amplifier current. This behavior is a natural consequence of the coexistence of two modes. Keeping both modes simultaneously at threshold requires particular values for the carrier densities in both DFB and amplifier section. Thus, both carrier densities are clamped in the two-mode regime. As a result, the contribution of the amplifier section to the feedback strength K becomes independent of the injection level [17]. Of course, the carrier densities are not constant but oscillate also with the beating frequency. However, the magnitude of the fluctuations around the threshold values is small and it makes sense to consider the average of K over one pulsation period. The situation changes in regime IV with irregular multimode pulsations. The slow components of these pulsations are accompanied with large variations of the carrier densities and, in turn, of K, making an average feedback strength meaningless here.

The numerical solution demonstrates that the AFL is capable of several dynamical regimes. However, a systematic understanding requires knowledge of the bifurcation diagram that underlies these results.

D. Bifurcation analysis

A very efficient method for constructing comprehensive bifurcation diagrams is path-following [18]. Well-developed path-following tools are available for ordinary differential equations [19] and, recently, also for delayed differential equations [20], but not for the traveling wave partial differential equations. Our subsequent approach is based on expanding the optical fields in terms of hot cavity modes [21,22]. Only the two master modes dominating the dynamics in a given island of self-pulsations are taken into account, as suggested by the numerical results of the preceding section. In addition, we ignore here LSHB ($N=\langle N\rangle$), gain dispersion ($\bar{g}=0$), as well as nonlinear gain saturation ($\varepsilon=0$) in the active sections. While yielding a less accurate description of the total mode spectrum, these simplifications reproduce the relations between the two closely spaced master modes sufficiently well and, thus, have only marginal influence on the dynamics of this subsystem [23,22]. As a result, the traveling wave equations (1)–(7) transform into a five-dimensional system of ordinary differential equations for two carrier densities and two complex mode amplitudes minus one irrelevant phase of the total optical field. These equations are now amenable for standard path-following methods [19].

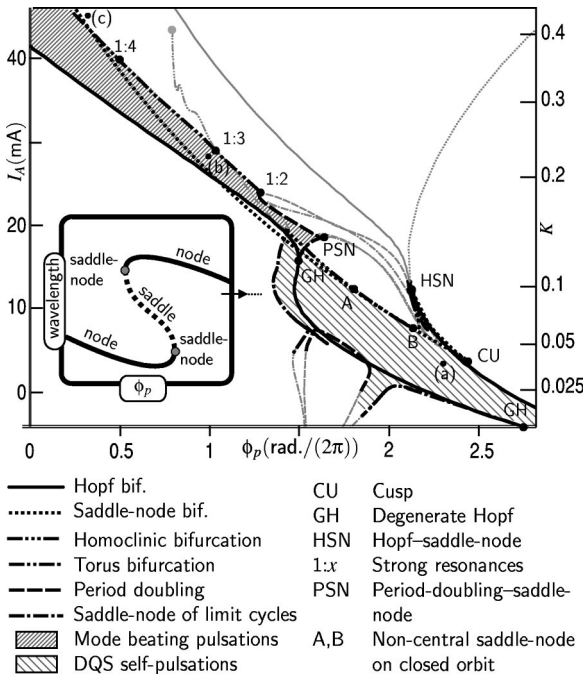

FIG. 4. Bifurcation curves and islands of stable self-pulsations of the simplified two-mode model in the parameter plane (ϕ_P, I_A). The shaded islands indicate stable DQS and MB self-pulsations. Parameter as in Table I except $\bar{g}=0$, $\varepsilon=0$, $\alpha_H=-4$. Furthermore α_P is fixed to 20 cm^{-1}, and LSHB and thermal detuning are neglected. Inset: wavelength of stationary states vs phase shift ϕ_P schematically illustrating the double-fold structure above the cusp. The right-hand scale is the feedback strength K at the lower Hopf bifurcation.

Figure 4 depicts in the (ϕ_P, I_A) parameter plane all bifurcations obtained for cw states and the most physically relevant bifurcations of self-pulsations.

The current axis is limited to the range where no more than two modes are dominant in the numerical solution of the full traveling wave equations. The shaded areas represent the islands of two different types of stable self-pulsations.

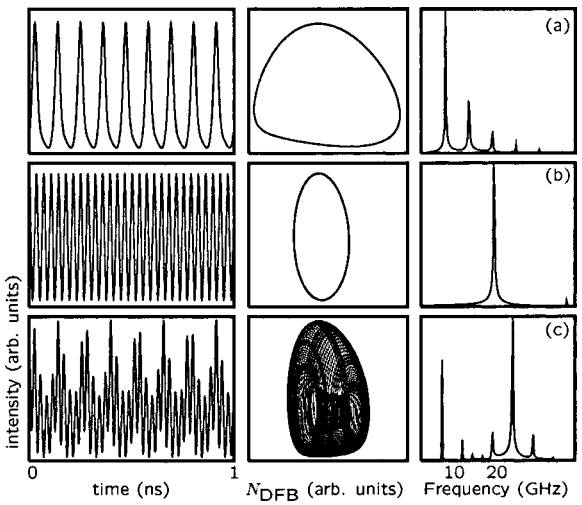

FIG. 5. Dynamics in the points labeled (a)–(c) of the bifurcation diagram in Fig. 4. (a) Typical low-frequency self-pulsation, (b) MB self-pulsation, and (c) beyond the torus bifurcation. Left column, output power vs time; middle column, projection of the phase space trajectory onto the plane of output power vs DFB carrier density, and right column, power spectrum.

The lower one with lighter shading corresponds to undamped single-mode relaxation oscillations. A typical pulse train, a projection of the periodic orbit, and a power spectrum of these so-called dispersive *Q*-switching (DQS) self-pulsations is shown in the first row of Fig. 5. MB self-pulsations appear in the upper island. An example is illustrated in the second row of Fig. 5. The two islands are tilted and extend over several phase periods. All these features agree very well with the corresponding structures in the equivalent part of Fig. 3 and also, as will be shown below, with the experimental findings. The extensions of the islands are somewhat larger than in the full numerical solution. This is mostly due to neglecting gain saturation by which the damping of the relaxation oscillations is underestimated. Recurring islands at higher periods of ϕ_P do not occur as only one selected pair of modes is considered. The good overall agreement of the two-mode approximation with the full numerical integration regarding the predicted self-pulsation areas makes it meaningful to examine the bifurcations of the AFL in more detail.

We start our discussion of the bifurcation diagram in Fig. 4 at the cusp point (CU), because it separates regions with a different number of cw states. The dotted line emanating from CU, one branch traversing to HSN (Hopf saddle-node), the other to *A* and *B*, represents a saddle-node bifurcation of cw states. At the dotted line, a saddle and a node are created, i.e., there are three cw states—two nodes and one saddle—between the two branches and only one cw state outside (cf. schematic inset of Fig. 4). The left branch of the curve and the right branch up to HSN involve at least one stable cw state. Hence, these branches represent boundaries of hysteresis regions. The numerical simulations of Sec. II C were performed for increasing ϕ_p, so that only the right branch of the saddle-node bifurcation was recognized as a mode jump.

The solid line represents a Hopf bifurcation of a cw state. A self-pulsation of small amplitude is born there. This self-pulsation is stable for the supercritical Hopf bifurcation above the upper generalized Hopf (GH) point and below HSN, and unstable for the subcritical Hopf bifurcation between the two GH points. In the experiment, a supercritical Hopf bifurcation will not show up as a sharp transition but as a slow rise of a peak at the Hopf frequency in the power spectrum. Opposed to this, a subcritical Hopf bifurcation is displayed by a discontinuity and could be the boundary of a hysteresis loop.

The physical mechanism destabilizing the laser mode at the Hopf boundary of the lower pulsation island is due to DQS, mediated by the gain-index coupling ($\alpha_H \neq 0$). Any fluctuation of the DFB inversion is accompanied by a wavelength change which in turn changes the quality factor of the feedback cavity. DQS has first been discussed and exploited in devices with a highly dispersive Bragg reflector in the feedback cavity [24,25]. It has also been predicted mathematically for lasers with a simple passive feedback [26]. Our present results confirm the conclusion that the intrinsic dispersion of an extended feedback cavity can be sufficient to cause DQS self-pulsations without an additional dispersive element.

The Hopf curve and the saddle-node curve touch each other in the point HSN. Above HSN, the cw state undergoing the bifurcations (both Hopf or saddle node) is unstable. Consequently, the bifurcation is not experimentally observable. The corresponding curves are shown in gray to indicate that they are of less interest.

Another boundary of the DQS self-pulsation area is due to homoclinic bifurcations represented by the triple-dot-dashed curve in Fig. 4. Here, the self-pulsation touches a cw saddle state and disappears. When moving across this curve, the frequency of the self-pulsation becomes smaller until the laser switches suddenly to a stable cw state. This switching occurs without hysteresis if the homoclinic connection in the phase space is actually towards a saddle node, i.e., if the curve of homoclinic bifurcations coincides with the curve of saddle nodes between points *A* and *B*. In this case, the stable cw state is excitable. Beyond *B*, the curve of homoclinics approaches the point HSN in a wiggling manner.

Apart from Hopf and homoclinic bifurcations, saddle nodes of limit cycles (single-dot-dashed line) and period-doubling bifurcations (dashed line) form the boundary of the DQS island. Period doubling is only the first step in a rapidly accumulating sequence leading to chaos within the region enclosed by the period doublings. The saddle-node limit cycle shrinks to zero at the upper GH point changing the Hopf bifurcation from subcritical to supercritical for increasing ϕ_P.

There is not much hysteresis with respect to parameter variation even at the subcritical Hopf bifurcation boundary of the DQS island between the two GH points. The reason is the proximity of the Hopf curve to the curves of period doubling and saddle nodes of limit cycles.

Our analysis also yields bifurcations that are not physically relevant. The phase-space trajectories related to some bifurcations leave the range of validity of the mode approximation. Other bifurcations involve unstable cw states or self-pulsations and, hence, are not experimentally observable. We show those parts in Fig. 4 in gray.

The MB pulsations are born on the Hopf bifurcation curve at higher amplifier current. A second mode reaches threshold here, whereas the relaxation oscillations remain strongly damped. Within the MB island, the power is distributed between the two modes such that they both keep at threshold. Further boundaries of this island are saddle nodes of limit cycles between the GH and PSN as well as period-doubling bifurcations between PSN and 1:2, and torus bifurcations represented by the double-dot-dashed line emerging from 1:2. Along most parts, the torus bifurcation is supercritical, i.e., a stable torus is born above this curve. This has been validated by several numerical tests. An example is drawn in the third row of Fig. 5. Both the fast MB oscillator and the slow relaxation oscillation are undamped here, giving rise to a modulated pulse train and a complex phase-space picture. A stable torus bifurcation does not manifest itself by a sharp transition in the experiments, but as a smooth rise of secondary peaks in the power spectrum below and above the main frequency peak. Close to the strong resonances (1:2, 1:3, 1:4), the secondary peaks are of low rational order and should be particularly pronounced.

For lasers with passive feedback [26,27], the island of MB pulsations generally forms only a narrow stripe in the parameter space in the case of a short external cavity. Apparently, the region of stable MB pulsations widens substantially with active feedback. Since the saddle-node bifurcation curve crosses this region, hysteretic behavior is expected in a large parameter range.

Concluding so far, two basic types of self-sustained intensity pulsations appear in active feedback lasers: slow relaxation oscillations undamped by DQS and fast MB pulsations due to the interplay of two compound cavity modes, reaching simultaneously the laser threshold.

III. EXPERIMENT

A. Device

The AFL, sketched in Fig. 1, is realized as an index-coupled multisection laser. It is designed for the 1550-nm window in fiber optical communication. The InGaAsP-InP bulk hetero structure is grown by low-pressure metal-organic vapor phase epitaxy. A 1550 nm InGaAsP layer as active zone is embedded in an asymmetric 1180 nm/1300 nm InGaAsP optical waveguide. Polarization independence of the optical gain is achieved by a suitable adjustment of the thickness of the layers and the strain in the active zone. The DFB grating is fabricated by *e*-beam lithography and reactive ion etching [5]. By adjusting properly the etching depth, a coupling coefficient of 130 cm^{-1} is achieved. The passive section is implemented as a 1300 nm structure by removing the 1550 nm active layer.

Figure 6 demonstrates how the phase shift can be tuned by changing the bias on the passive section. The dark lines are the resonances of the amplified spontaneous emission (ASE) detected at the amplifier facet, while fixing the DFB current to transparency level (8.6 mA) and pumping the amplifier section with 45 mA. These data are used below to translate the applied phase current I_p into the actual phase shift ϕ_P. The observed ASE resonances correspond to the

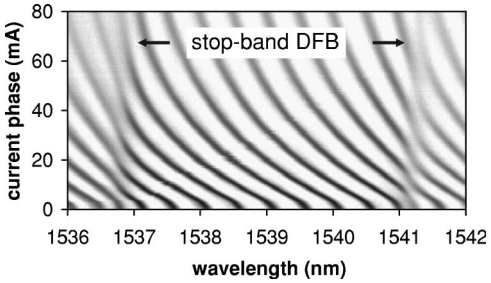

FIG. 6. ASE measured at the amplifier facet with the DFB section pumped at transparency. The cavity between end facet and DFB grating allows for a verification of the phase shift in the passive section. The excessive loss by free-carrier injection causes the damping of the ASE modulation with increasing current.

damped FP-type modes found in the mode analysis of Sec. II B. The 0.42 nm average spacing compares very well with the calculations. At the stop-band edges, the spacing is reduced due to stronger dispersion of the grating reflectivity. Apart from the refractive index, also the free-carrier absorption is changed by current injection into the passive section. An evaluation of the ASE modulation depth gives an excess loss of about 4 cm^{-1} per phase period in the current range investigated.

B. Regions of nonstationary emission

Optical and power spectra of the AFL output were recorded at the amplifier facet. An optical spectrum analyzer Advantest Q8384A and an electrical spectrum analyzer HP8565E were used. A fast u2t photodiode (uZt photonics AG, http:www.uZt.de), postamplified by a HP83050A electrical amplifier (50 GHz bandwidth) served as optoelectronic converter. To reduce the parameter space, the DFB current was fixed to 70 mA (about two times the threshold current of the solitary DFB) at a device temperature of 20°C. Phase current and amplifier current were varied from 0 to 50 mA and from 0 to 100 mA, respectively.

Figure 7 summarizes the result of the measurements in a similar contour plot as used to present the numerical calculations in Fig. 3. In the areas of nonstationary output, the power spectra exhibit peaks at nonzero frequencies with intensities exceeding the noise level by more than 10 dB. The very good agreement between theory and experiment is evident. Deviations are mainly caused by uncertainties concerning the translation of experimental currents into more fundamental parameters such as feedback strength. The shift of the whole plot to higher amplifier currents is mainly attributed to higher losses in the feedback cavity than used in the numerical solution.

In what follows, we focus more closely on the role of the active feedback by keeping the phase current fixed (8 mA). The vertical cross sections marked in Fig. 7 proceed through regions of low- and high-frequency self-pulsations and contain spectral features that are representative for the whole parameter plane.

C. Undamped DQS relaxation oscillations

Figure 8 depicts spectra typical for the regions of low-frequency self-pulsations. The power spectrum with a main

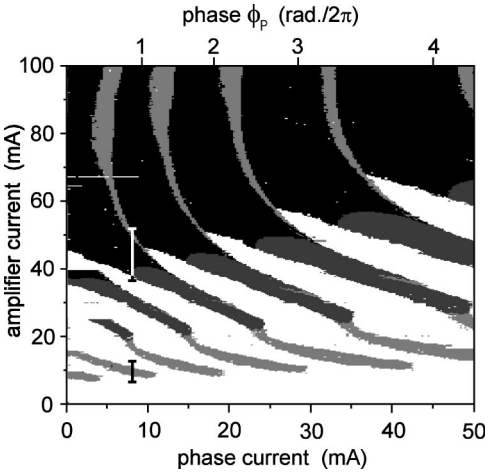

FIG. 7. Areas of self-pulsations in the plane of phase and amplifier current. DFB current is fixed at 70 mA. For comparison with the numerical results, ϕ_P is given at the top axis. The gray scale is the same as in Fig. 3. Only the frequency component with highest intensity is indicated. The vertical bars mark regions, where more details are presented in the subsequent figures.

frequency of 9 GHz and a distinct second harmonic at 18 GHz compares well with the theoretical spectrum in Fig. 5(a). The optical spectrum shows a splitting of the emission line into several subcomponents with a spacing corresponding to the 9 GHz pulsation frequency. These features are characteristic for DQS-type self-pulsations derived theoretically above.

According to the calculated bifurcation diagram (Fig. 4), the main boundaries of the DQS-pulsation regions are either Hopf or homoclinic bifurcations. In order to verify this prediction, the amplifier current was tuned across the island region. The inset in Fig. 8 shows the evolution of height and position of the primary peak of the power spectrum. The steep but continuous increase of the peak height at about $I_A=9$ mA is consistent with a supercritical Hopf bifurcation of the relaxation oscillations, which are driven by spontaneous emission noise. When approaching this bifurcation, the damping of the oscillations goes to zero, while the peak increases exponentially. During the bifurcation, the frequency changes continuously, too. After a slight increase, a distinct slowing down is observed, which is accompanied by a further increase of the peak height. Both observations indicate an expansion of the periodic orbit of the pulsation in the plane of carrier vs photon density. In contrast to the smooth onset the pulsations abruptly disappear at the upper island boundary by a sudden jump to a longer-wavelength mode. Such behavior is consistent with a homoclinic bifurcation above *A* in Fig. 4. Due to the exponentially small region of the homoclinic, only a moderate slow down of the pulsation frequency towards this bifurcation occurs. Fluctuations, unavoidable in the experiment, prevent a sufficiently smooth approach to the homoclinic, disabling the observation of $f\rightarrow 0$.

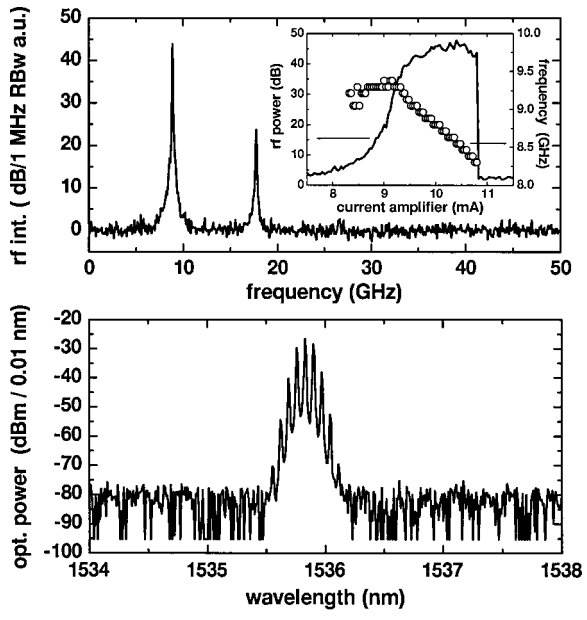

FIG. 8. Power (upper panel) and optical (lower panel) spectrum ($I_{DFB}=70$ mA, $I_P=8$ mA, $I_A=9$ mA). Inset: evolution of the primary peak of the power spectrum with increasing amplifier current I_A. Solid line, peak height; circles, frequency. Note the log scale. All rf measurements with 1 MHz resolution bandwidth (RBw).

D. Mode-beating pulsations

Figure 9 shows the evolution of spectra at higher amplifier currents. Below $I_A=47$ mA, the power spectrum consists of a single line at about 30 GHz in good agreement with the theoretical prediction of stable MB pulsations. Possible higher harmonics are beyond the bandwidth of the spectrum analyzer. The frequency remains nearly unchanged in the range of pure MB. This is consistent with the independence of the feedback strength *K* on the amplifier current within the respective MB islands (see Fig. 3).

A typical optical spectrum of a MB pulsation is drawn for $I_A=40$ mA in Fig. 9. Two central peaks of comparable height are accompanied by one or more pairs of satellites. The central peaks represent the coexisting pair of optical modes. Their separation of 0.25 nm corresponds to the beating frequency of 30 GHz and it is considerably reduced relative to the 0.4 nm FP separation. This reduction is due to the mode pulling effect at the DFB resonances already discussed above. The satellites, separated from the main peaks by the same spacing, are due to nondegenerate four-wave mixing of the two coexisting modes. The presence of such intense mixing products signifies a good spatial overlap of the two modes within the device and high phase stability of the MB pulsations.

In accordance with a supercritical Hopf bifurcation the onset of the MB pulsations is a continuous transition, smoothed by the presence of noise. The optical spectrum at $I_A=36$ mA shows already the second mode being close to threshold. It is only weakly damped here and can collect a measurable amount of spontaneous emission. With increasing amplifier current, this peak rises quickly and approaches the height of the first one at about $I_A=38$ mA.

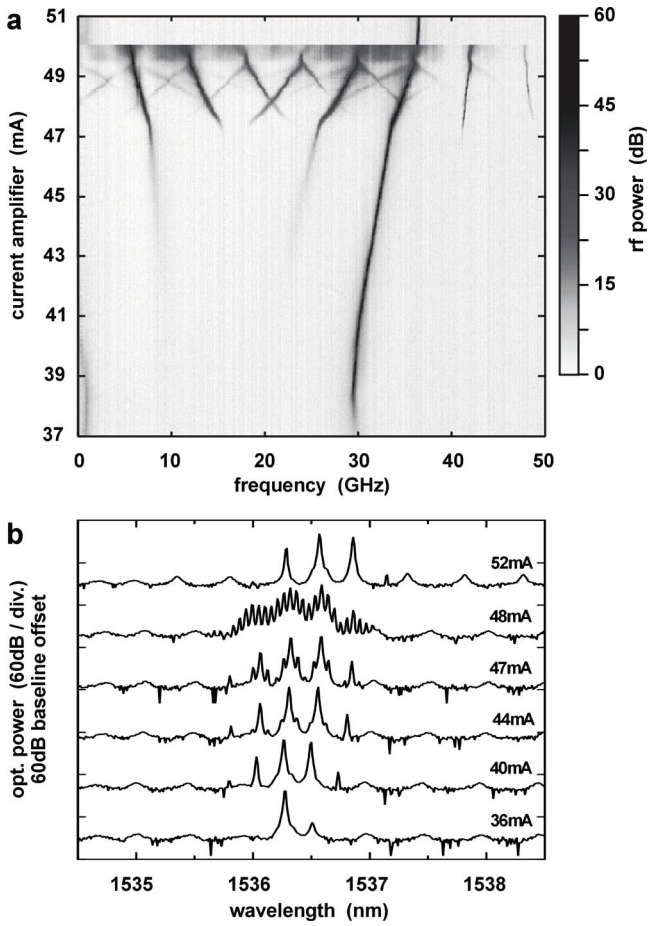

FIG. 9. Characteristic spectra at high amplifier currents ($I_{DFB}=70$ mA, $I_P=8$ mA). Panel (a): power spectrum for I_A from 37 to 51 mA. The logarithmic gray scale codes the spectral intensity as denoted on the right-hand side. Panel (b): log-scale optical spectra at selected points of panel (a). Pure MB pulsation appears below $I_A=47$ mA, whereas the more complex spectral features above this amplifier current are due to the interaction between the relaxation oscillations and MB pulsations.

E. Torus of mode-beating and relaxation oscillations

The scenario at the upper boundary of the MB pulsation region is more complex. A new low-frequency component emerges at about $I_A=47$ mA in the power spectrum [Fig. 9(a)] and coexists with the MB component. It has noticeable higher harmonics and causes mirror satellites of the MB line indicating a nonlinear interaction between both components. These phenomena are characteristic attributes of the torus bifurcation predicted by theory. Again, the transition is continuous indicating supercritical character. Weak shoulders of the main features, already present in the optical spectra at $I_A=44$ mA, are precursors of this bifurcation. The shoulders become increasingly prominent and dissolve in individual sublines in the torus region, starting at about $I_A=48$ mA. The frequency of the emerging new component in the power spectrum is slightly below 10 GHz. This points at relaxation oscillation as physical origin of the torus. However, contrary to the standard case, where a cw state is approached, this relaxation leads towards a periodic orbit formed by the two

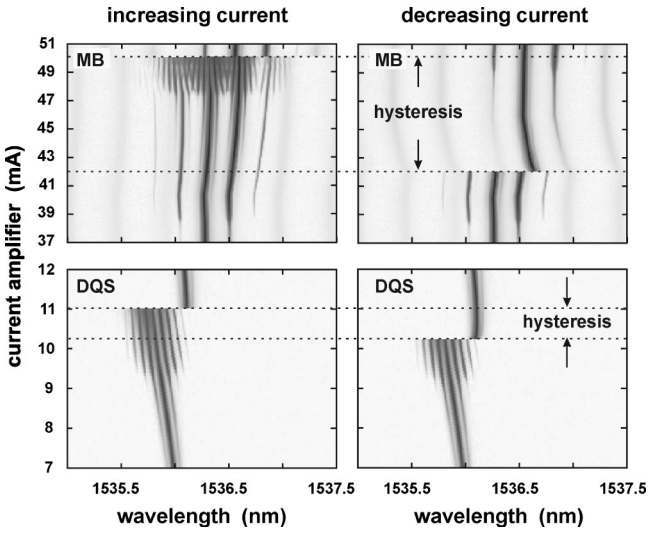

FIG. 10. Comparison of optical spectra for increasing (left) and decreasing amplifier current (right) for the DQS and MB ranges indicated in Fig. 7 ($I_P=8$ mA). The optical intensity is encoded in logarithmic gray scale.

coexisting dominant modes. Below the torus bifurcation, such oscillations are excited by internal or external noise, perturbing the power distribution between the two modes, at which they are both at threshold. Above the torus bifurcation, these distribution oscillations become undamped and create a cyclic variation of the modulation depth as depicted in the lower left panel of Fig. 5.

The details of the power spectra in the torus region between $I_A=47$ and 50 mA uncover a sequence of further bifurcations, which were not obtained by the mathematical analysis of Sec. II D. Just above $I_A=49$ mA, the two frequency components synchronize to each other at a 1:6 ratio within a 300 μA current range. For other phase currents, we could observe similar synchronized states with different integer frequency ratios. However, a detailed description and analysis of these phenomena is beyond the scope of this paper. Above the locking region, an additional broad background band appears. This band is related to a chaotic component in the AFL dynamics, probably due to participation of a third mode. It dominates the spectrum until the laser jumps suddenly to a beating state of the next pair of modes with higher pulsation frequency than in the previous island. This observation is also consistent with the predictions of Fig. 3. Note that the feedback strength switches to a higher level when moving vertically from one island to the next one.

F. Hysteresis

Some of the bifurcations elaborated in Sec. II D are associated with hysteresis behavior. Figure 10 compares optical spectra in the DQS and MB regime for increasing and decreasing amplifier current, respectively. Indeed, both data sets clearly exhibit hysteresis.

In the DQS case, the onset of pulsation in the backward direction is shifted with respect to increasing current by about 1 mA. The presence of hysteresis provides strong evidence that the AFL operates above point *A* in Fig. 4, so that

the different locations of the saddle-node bifurcation and homoclinic produce this behavior. Note that the switching in forward and backward directions occurs at the same feedback strength.

The MB regime differs from these observations mainly in the width of the hysteresis. While the lower switching point is not affected by the direction, the upper current level, where the pulsations disappear, is shifted by 8 mA. Due to this shift, the torus scenario observed for increasing amplifier current direction is entirely absent. The reason is again a saddle-node bifurcation, which is located below the bifurcation responsible for the torus pulsations (Fig. 4). The onset of the same MB pair in backward direction at the saddle-node bifurcation produces a large hysteresis range in I_A. A further factor increasing the hysteresis range is the slow variation of the feedback strength K in the MB regime, as seen in Fig. 3.

IV. SUMMARY

Using the AFL as a device, the nonlinear dynamics in the very short-cavity limit has been studied. Separate control of feedback phase and strength allowed us to adjust the number of relevant laser modes and to prepare well-defined dynamical scenarios. Two regimes dominate the device behavior. In the low-feedback range ($K \leqslant 0.1$), the dynamics is governed by a single mode. Instabilities of this mode result in DQS pulsations, without the need of an additional dispersive element. At higher feedback levels, available through the introduction of the amplifier section, distinct MB pulsations originating from a pair of compound modes occur. Hysteresis due to homoclinic and saddle-node bifurcations is observed. When the feedback strength is further increased, both types of pulsations coexist, giving rise to new effects, e.g., internal synchronization. The bifurcation diagram predicts a broad range of further phenomena typical for the very short-cavity regime. All these features make the AFL an ideal candidate for the investigation of systems with delayed optical feedback.

ACKNOWLEDGMENTS

The work of J. S., H.-J.W., and F. H. was performed in the framework of Grant No. Sfb 555 funded by the Deutsche Forschungsgemeinschaft (DFG). The work of M.R. was supported by DFG Research Center ''Mathematics for key technologies'' (Grant No. FZT 86) in Berlin, Germany. The authors thank B. Krauskopf for a critical reading of the manuscript.

[1] I. Fischer, T. Heil, M. Münkel, and W. Elsässer, Proc. SPIE **3283**, 571 (1998).
[2] H.-J. Wünsche, O. Brox, M. Radziunas, and F. Henneberger, Phys. Rev. Lett. **88**, 023901 (2002).
[3] B. Krauskopf, K. Schneider, J. Sieber, S. Wieczorek, and M. Wolfrum, Opt. Commun. **215**, 367 (2002).
[4] M. Giudici, C. Green, G. Giacomelli, U. Nespolo, and J. Tredicce, Phys. Rev. E **55**, 6414 (1997).
[5] M. Möhrle, B. Sartorius, C. Bornholdt, S. Bauer, O. Brox, A. Sigmund, R. Steingrüber, M. Radziunas, and H.-J. Wünsche, IEEE J. Sel. Top. Quantum Electron. **7**, 217 (2001).
[6] J. Ohtsubo, IEEE J. Quantum Electron. **38**, 1141 (2002).
[7] T. Heil, I. Fischer, W. Elsässer, and A. Gavrielides, Phys. Rev. Lett. **87**, 243901 (2001).
[8] T. Heil, I. Fischer, W. Elsässer, B. Krauskopf, K. Green, and A. Gavrielides, Phys. Rev. E **67**, 066214 (2003).
[9] A.A. Tager and K. Petermann, IEEE J. Quantum Electron. **30**, 1553 (1994).
[10] S. Bauer, O. Brox, J. Kreissl, G. Sahin, and B. Sartorius, Electron. Lett. **38**, 334 (2002).
[11] R. Lang and K. Kobayashi, IEEE J. Quantum Electron. **16**, 347 (1980).
[12] M. Radziunas, H.-J. Wünsche, B. Sartorius, O. Brox, D. Hoffmann, K. Schneider, and D. Marcenac, IEEE J. Quantum Electron. **36**, 1026 (2000).
[13] U. Bandelow, M. Wolfrum, M. Radziunas, and J. Sieber, IEEE J. Quantum Electron. **37**, 183 (2001).
[14] P.G. Eliseev, A.G. Glebov, and M. Osinski, IEEE J. Sel. Top. Quantum Electron. **3**, 499 (1997).
[15] U. Bandelow, H.-J. Wünsche, B. Sartorius, and M. Möhrle, IEEE J. Sel. Top. Quantum Electron. **3**, 270 (1997).
[16] A.A. Duarte and H.G. Solari, Phys. Rev. A **60**, 2403 (1999).
[17] O. Brox, S. Bauer, M. Radziunas, M. Wolfrum, J. Sieber, J. Kreissl, B. Sartorius, and H.-J. Wünsche, IEEE J. Quantum Electron. **11**, 1381 (2003).
[18] B. Krauskopf, in *Nonlinear Laser Dynamics: Concepts, Mathematics, Physics, and Applications, International Spring School*, edited by Bernd Krauskopf and Daan Lenstra, AIP Conf. Proc. No. 548 (AIP, Melville, New York, 2000), p. 1.
[19] E.J. Doedel, A.R. Champneys, T.F. Fairgrieve, Y.A. Kuznetsov, B. Sandstede, and X. Wang, *AUTO97, Continuation and Bifurcation Software for Ordinary Differential Equations* (Concordia University, Montreal, Canada, 1998).
[20] K. Engelborghs, T. Luzyanina, and D. Roose, ACM Trans. Math. Softw. **28**, 1 (2002).
[21] H. Wenzel, U. Bandelow, H.-J. Wünsche, and J. Rehberg, IEEE J. Quantum Electron. **32**, 69 (1996).
[22] J. Sieber, SIAM J. Appl. Dyn. Sys. **1**, 248 (2002).
[23] M. Radziunas and H.-J. Wünsche, Proc. SPIE **4646**, 27 (2002).
[24] V. Tronciu, H.-J. Wünsche, J. Sieber, K. Schneider, and F. Henneberger, Opt. Commun. **182**, 221228 (2000).
[25] B. Sartorius, M. Möhrle, S. Reichenbacher, H. Preier, H.-J. Wünsche, and U. Bandelow, IEEE J. Quantum Electron. **33**, 211 (1997).
[26] M. Wolfrum and D. Turaev, Opt. Commun. **212**, 127 (2002).
[27] T. Erneux, F. Rogister, A. Gavrielides, and V. Kovanis, Opt. Commun. **183**, 467 (2000).